Journal of Energy Chemistry 65 (2022) 116–126

Contents lists available at ScienceDirect

Journal of Energy Chemistry

journal homepage: www.elsevier.com/locate/jechem

http://www.journals.elsevier.com/journal-of-energy-chemistry/

One-pot hydrothermal preparation of hierarchical manganese oxide nanorods for high-performance symmetric supercapacitors

Bidhan Pandit [a,*], Emad S. Goda [b,c,*], Mahmoud H. Abu Elella [d], Aafaq ur Rehman [e], Sang Eun Hong [b], Sachin R. Rondiya [f], Pranay Barkataki [g], Shoyebmohamad F. Shaikh [h], Abdullah M. Al-Enizi [h], Salah M. El-Bahy [i], Kuk Ro Yoon [b]

[a] Department of Materials Science and Engineering and Chemical Engineering, Universidad Carlos III de Madrid, Avenida de la Universidad 30, 28911 Leganés, Madrid, Spain
[b] Organic Nanomaterials Lab, Department of Chemistry, Hannam University, Daejeon 34054, Republic of Korea
[c] Fire Protection Laboratory, National Institute of Standards, 136, Giza 12211, Egypt
[d] Chemistry Department, Faculty of Science, Cairo University, Giza 12613, Egypt
[e] Graduate School of Energy Science and Technology, Chungnam National University, 99 Daehak-ro, Yuseong-gu, Daejeon 34134, Republic of Korea
[f] School of Chemistry, Cardiff University, Main Building, Park Place, Cardiff, CF10 3AT Wales, United Kingdom
[g] Department of Physics, Visvesvaraya National Institute of Technology, South Ambazari Road, Nagpur-440010, Maharashtra, India
[h] Department of Chemistry, College of Science, King Saud University, P.O. Box 2455, Riyadh 11451, Saudi Arabia
[i] Department of Chemistry, Turabah University College, Taif University, P.O. Box 11099, Taif 21944, Saudi Arabia

ARTICLE INFO

Article history:
Received 26 January 2021
Revised 29 April 2021
Accepted 20 May 2021
Available online 26 May 2021

Keywords:
α-MnO_2 nanorods
Rietveld refinement
Symmetrical supercapacitors
High energy density

ABSTRACT

An eco-friendly, new, and controllable approach for the preparation of manganese oxide (α-MnO_2) nanorods has been introduced using hydrothermal reaction for supercapacitor application. The in-depth crystal structure analysis of α-MnO_2 is analyzed by X-ray Rietveld refinement by using FullProf program with the help of pseudo-Voigt profile function. The developed α-MnO_2 electrode attains a remarkable capacitance of 577.7 F/g recorded at a current density value of 1 A/g with an excellent cycle life when is used for 10,000 repeated cycles due to the porous nanorod-morphology assisting the ease penetration of electrolyte ions into the electroactive sites. The diffusive and capacitive contributions of the electrode have been estimated by considering standard numerical packages in Python. After successfully assembling the aqueous symmetric supercapacitor (SSC) cell by utilizing the as-prepared α-MnO_2, an excellent capacitance of 163.5 F/g and energy density of 58.1 Wh/kg at the constant current density of 0.5 A/g are obtained with an expanded potential frame of 1.6 V. Moreover, the cell has exceptionally withstood up to 10,000 cycles with an ultimate capacitance retention of 94.1% including the ability to light an LED for 18 s. Such findings recommend the developed α-MnO_2 electrode to be a highly felicitous electrode for the field of energy storage.

1. Introduction

Nowadays, the urgent need for electric vehicles and portable electronic devices has been rapidly increased in various applications leading to the great motivation for exploring numerous energy storage systems with high energy/power density [1–5]. Supercapacitors (SCs) are counted as important electrochemical energy storage technologies featuring prompt charge/discharge processes, eminent power density, and stable cycling behavior [6,7]. Consequently, they can easily fill out the space presented between the redox chemical battery and traditional capacitors. As a result, fast prosperity in the supercapacitor research is noticed where the attentiveness is mainly destined toward the preparation of advanced electrodes with low-cost and high efficient properties [8–10]. Notably, the active electrode material is essentially chosen based on the intended application and the mechanism of action for storing the charge. The electric double-layer capacitance (EDLC) is achieved by carbon containing electrodes (such as activated carbon, carbon nanotubes, graphene) where the charge is usually stored through adsorption and desorption processes of electrolyte ions without involving any redox reaction [11,12]. However, the pseudocapacitance is considered by the rapid reversible redox-based reactions that occur normally in metal oxides and conducting polymer-based materials [13–15]. Generally, the capacitance

* Corresponding author.
E-mail addresses: physics.bidhan@gmail.com (B. Pandit), emadzidan630@gmail.com (E.S. Goda).

https://doi.org/10.1016/j.jechem.2021.05.028

produced by the carbonaceous materials is recorded lower as compared to the redox-based electrode materials [16].

Since the premier battery of Zn-MnO_2 was explored by Leclanché in 1866, various oxides of transition metals have been successfully applied as capacitor electrodes such as NiO, MoO_2, and Co_3O_4 [17–20]. Particularly, MnO_2 is commonly exploiting in rechargeable batteries and supercapacitors as a result of its outstanding features including great theoretical capacitance ability (1370 F/g), cost-effectiveness, and non-toxicity, offering a good capacitance efficiency and speedy reversibility in redox reactions with a broad potential window for aqueous electrolytes [21]. Nevertheless, MnO_2 possesses the shortness of a rapid charge–discharge rate coming from the lower conductivity and is responsible for the occurrence of redox process on the electrode surface and the limitation of electrolyte ions from passing through the internal channels of the working electrode leading to the depletion of the electrochemical behavior [22,23]. As a solution, the electrochemical manner of MnO_2 can be improved by controlling important aspects such as the morphology, crystalline nature, surface area, and size diameter to enhance the electrochemical kinetics and thermodynamic features [10,24,25]. The previously developed capacitors of MnO_2 with various morphology shapes such as particles, spheres, and flowers could assure the efficient capacitance activity due to the boosted electroactive area of the working electrode and hence were able to achieve more interfacial interaction and fasten the kinetics between the electrode and electrolyte ions [26,27]. Numerous methods such as microemulsion, template-based, and co-precipitation have been utilized to design several MnO_2 nanoarchitectures [28–30]. However, some routes reported for the MnO_2 synthesis are very complicated and hard to control the size and shape considering the over-growth and agglomeration difficulties [24]. Whereas the hydrothermal technique is recognized as an effective chemical approach for obtaining nanostructures with a high surface area, and a well-defined structure due to the facile control of the synthesis factors such as pressure, time, and most importantly temperature.

Herein, for the first time, an efficient and size controllable system for the development of α-MnO_2 nanorods by proceeding hydrothermal oxidation of manganese precursors with ammonium persulfate in a basic medium is applied for the symmetric supercapacitor (SSC) application. The developed method is found to give one-dimensional α-MnO_2 without using any complicated or expensive template agents. Besides, the easy surface accessibility and mended electrochemical behavior of the electrode were certainly produced from the high surface area coming from the as-prepared nanorods that can provide both the highly reversible pseudocapacitance and capacitive retention ratio with a higher charge–discharge rate. As expected, the electrode exhibits the utmost specific capacitance of 577 F/g calculated while applying the scan rate of 5 mV/s. Moreover, the constructed symmetric supercapacitor possesses a maximum energy density of 58.1 Wh/kg at a power density of 0.8 kW/kg and also shows a superior long cycle life, with ~ 94.1% capacitance retaintion after cycling of 10,000 times. The simplicity of the approach and excellent electrochemical properties can open a way for energy storage application integrated with industry-scalable strategy.

2. Experimental

2.1. Synthesis of α-MnO_2 nanorods

α-MnO_2 was primarily synthesized from the chemical oxidation of manganese precursor (manganese (II) acetate) using ammonium persulfate in an alkaline solution (Fig. 1). In brief, 100 mL of aqueous solution from sodium hydroxide was firstly adjusted at 0.2 M concentration and subsequently split into two beakers evenly. After that, sodium hydroxide solutions were mixed separately with 0.2 M manganese acetate and 0.4 M ammonium persulfate and were left to stir for an hour. The ammonium persulfate solution was progressively mingled with the other manganese precursor, and the obtained mixture was placed into the teflon-lined stainless-steel autoclave and thermally treated at 180 °C for 12 h. After reaching the room temperature, a brown precipitate was filtered, washed with a plenty of ethanol, and dried subsequently in the air at 60 °C for 24 h. Finally, the product was further calcined at 300 °C for 4 h in air to get the α-MnO_2 nanorods (MONRs).

Our design for the preparation of manganese dioxide contains two chemical reactions. In the first reaction, manganese hydroxide compound was formed by the reaction of sodium hydroxide with the manganese precursor:

$$(CH_3COO)_2Mn + 3OH^- = Mn(OH)_3^- + 2CH_3COO^- \quad (1)$$

While, the second one involves an oxidoreduction reaction between the persulfate anions and manganese hydroxide based on the following equation:

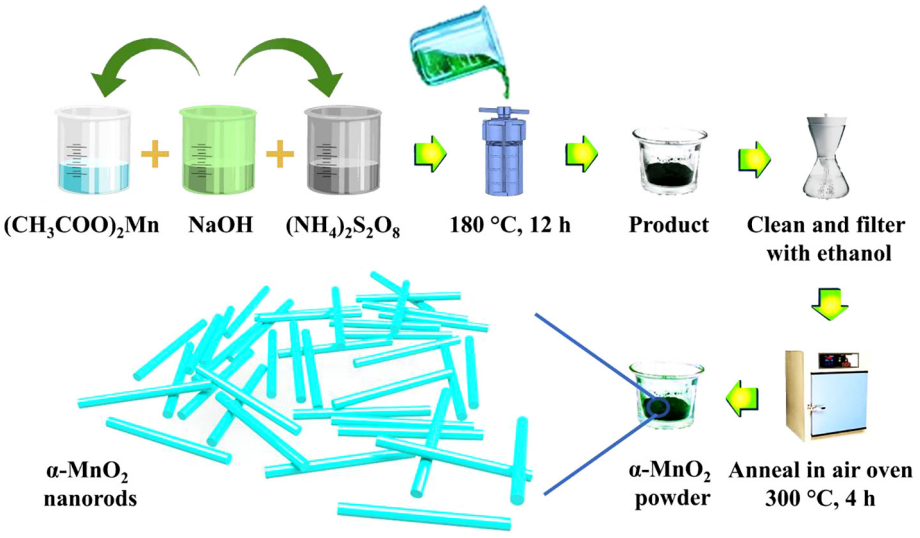

Fig. 1. Scheme of α-MnO_2 synthesis.

$$Mn(OH)_3^- + S_2O_8^{2-} + OH^- = MnO_2 + 2SO_4^{2-} + 2H_2O \quad (2)$$

2.2. Characterizations

D8 Advance Bruker was engaged to record X-ray diffraction (XRD) of the prepared sample with Cu K_α (λ = 1.5406 Å) radiation. Raman spectroscopy was performed using LabRAM HR system with 532 nm laser source. Furthermore, XPS analysis was performed using ThermoElectron ESCALAB 250 spectrometer with Al K_α radiation (1486.6 eV). The Brunauer-Emmett-Teller (BET) surface area and Barrett-Joyner-Halenda (BJH) pore size distribution of as-prepared sample were analyzed by N_2 adsorption–desorption test (Belsorb apparatus). The morphology and atomic composition of the nanorod structure were examined using field emission scanning electron microscopy (FESEM) and high resolution transmission electron microscopy (HRTEM) through running the Hitachi S-4800 and FEI TECNAI G2 20 Twin instruments, respectively. The CV current contributions (diffusive and capacitive) were numerically calculated for every constant potential point using Python script with standard numerical library sklearn. Linear regression method was used to fit (linearly) the datapoints plotted between the axes $i(V)/v^{1/2}$ (Y axis) vs. $v^{1/2}$ (X axis).

2.3. Electrochemical measurements

The α-MnO_2 sample was ground well in a mixture of activated carbon, and polyvinylidene fluoride with the mass ratio 8:1:1 and were subsequently dispersed in *N*-methyl-2-pyrrolidinone solvent for 1 h. The resultant solution was then dropped on well-cleaned nickel foam of 1 cm × 1 cm. The electrode was then dried overnight in vacuum oven and was utilized as the working electrode. The electrochemical behavior for α-MnO_2 electrode was investigated on potentiostat with the model of AutoLab (PGSTAT128N, Metrohm) in 1 M Na_2SO_4 electrolyte. Besides, Ag/AgCl and platinum wire were set as the reference and counter electrodes, respectively.

For further exploring the merits of as-prepared α-MnO_2 electrode, a symmetrical device was fabricated in the aqueous 1 M Na_2SO_4 electrolyte. The associated electrode mass deposited on nickel foams was found to be 0.5 mg for 1 cm × 1 cm substrate. The specific capacitance from cyclic voltammetry (C_v: F/g), and Galvanostatic charge–discharge curve (C_g: F/g), power density (P_d: W/kg), and energy density (E_d: Wh/kg) were measured based on standard equations (Supporting discussion).

3. Results and discussion

3.1. Structural and morphology characterization of the as-prepared α-MnO_2

The high-resolution powder XRD pattern along with Rietveld refinement by pseudo-Voigt function (FullProf program) for α-MnO_2 is depicted in Fig. 2(a), confirming the tetragonal crystalline structure of α-MnO_2 with reference to JCPDS #44–141. The observable diffraction peaks situated at 2θ of 12.7°, 18.1°, 25.6°, 28.7°, 37.5°, 41.9°, 49.7°, 55.9°, 60.0°, 65.1°, 69.1°, and 72.7° correspond to the crystallographic planes of 110, 200, 220, 310, 211, 301, 411, 600, 521, 002, 541, and 312, consecutively. Rietveld refinement performed for the lattice parameters and profile coefficients uncovers that our method offers a good consistency between the experimental data (black spheres) and calculated model (red line) for the I4/m space group. Also, the cell parameters from the Rietveld refinements were estimated as a = 9.896789 Å, b = 9.896789 Å and c = 2.858395 Å with angle $\alpha = \beta = \delta$ = 90°, corresponding to a cell volume of 279.970 Å^3 for the α-MnO_2. All the refinement parameters are summarized in Table 1 and 2. The tetragonal α-MnO_2 crystal structure as shown inset Fig. 2(a) is created in edge-sharing structure with corner of manganese octahedral (MnO_6) units and can offer enough space for electrolyte ions to improve the electrochemical properties.

Meanwhile, the structure of as-prepared α-MnO_2 was further identified using the Raman technique as shown in Fig. 2(b) which reveals four bands found at 176, 514, 582, and 632 cm^{-1} assigned for the α-type of manganese dioxide phase. For α-MnO_2, there should be 15 spectroscopic Raman modes for describing their structure which are 6Ag, 6Bg, and 3Eg [31] but they cannot be fully detected in the polycrystalline structure as realized in our developed material (only detectable four peaks). The clear bands at the frequency of 582 and 632 cm^{-1} are recognized to the vibration of symmetrical Mn–O vibrations and the spectroscopic modes that conform the well-grown of a tetragonal structure from α-MnO_2 with an interstitial space. Moreover, the lower-frequency band of 176 cm^{-1} is for the external translational vibration of the MnO_6 octahedra concerned with the tunnel ions [32,33].

On the other hand, the XPS was employed to identify the structural insights of the as-synthesized nanorods. The peaks of Mn, O, N, and C are clearly detected in the XPS survey spectrum of α-MnO_2 as shown in Fig. 2(c). Additionally, the inclusion of tiny Na 1*s* and Na KL1 peaks are coming from the NaOH precursor used during the preparation of α-MnO_2. The survey spectrum matches with the previously reported studies [34–36]. The core level XPS spectra of Mn 2*p* and O1*s* are shown in Fig. 2(d and e). As can be seen from Fig. 2(d), the Mn 2*p* spectrum is split into spin doublet peaks pointed at 641.9, and 653.6 eV which correspond to 2*p*3/2 and 2*p*1/2, respectively. It is apparent that the difference in binding energy between the above-assigned peaks of Mn 2*p* is found to be 11.7 eV that conforms that the manganese in α-MnO_2 has the oxidation state of + 4 [37,38]. Whereas, O 1*s* spectrum is found in Fig. 2(e) that shows two different surface oxygen species located at the binding energies of 529.6 eV corresponding to the lattice oxygen coded as O_α, and 531.1 eV which is attributable to the defected oxide or the oxygen ions existed in the low coordination situation (denoted as O_β) of the α-MnO_2 surface [39].

The nitrogen adsorption–desorption results as depicted in Fig. 2 (f) indicate that the α-MnO_2 nanorods exhibit a BET surface area of 34.5 m^2/g. Moreover, pore size distribution plot acquired from the desorption part (inset of Fig. 2f) of BJH isotherm uncovers an average pore size of ~ 33 nm. The hierarchical nanorod morphology with precise porous structure is beneficial for improved electrochemical properties as open structure and large surface area provide more electroactive sites for chemical reactions, minimize the ion diffusion lengths and enable quick ion transportation [40,41].

The surface morphology for the as-prepared α-MnO_2 was also inspected by doing FESEM and HRTEM analysis as depicted in Fig. 3. They appeared with well uniform grown one-dimensional nanorod crystals with a length range from 160–350 nm as indicated in FESEM images in Fig. 3(a and b), and a diameter of 10 nm as calculated from the HRTEM images in Fig. 3(c and d). This morphology can have merits for the electrode that need fast surfacial reactions giving the chance for the electrolyte ions to access the electrode interlayers leading to achieving an enhanced capacitance behavior for MONRs [24]. Selected area electron diffraction (SAED) pattern seen in Fig. 3(e) approves the polycrystallinity of α-MnO_2 and the well-defined crystalline planes can be indexed to the 200, 310, 211, 301, 411, 521, 002, and 541 planes of α-MnO_2 (JCPDS, card no: 44–141), showing good agreement with specified peaks of XRD pattern. Additionally, the elemental mapping spotted in Fig. 3(f–h) shows the formed MONRs with a homogenous surface architecture, in which the uniform dispersion

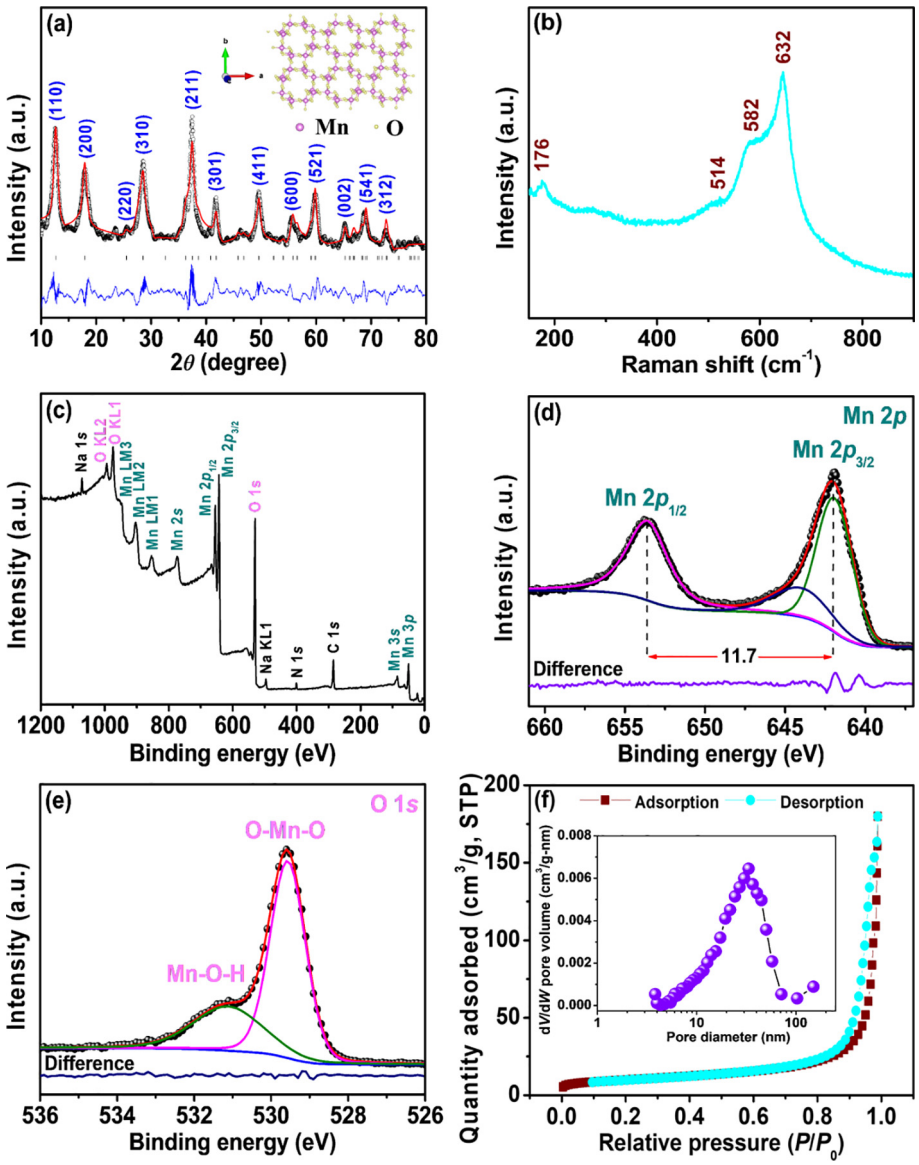

Fig. 2. (a) XRD spectrum of α-MnO_2. (b) Associated Raman pattern. (c) Survey level XPS spectrum of α-MnO_2 sample. (d and e) XPS spectra deconvolution of core level spectra for Mn 2*p* and O 1*s*. (f) Nitrogen adsorption/desorption isotherm curve of α-MnO_2 (inset displays the BJH pore size distribution plot).

Table 1
Structural parameters analyzed by Rietveld refinements for α-MnO_2.

Formula [molecular weight (g/mol)]	MnO_2 [86.937]
Crystal system	Tetragonal
Space group	I4/m (#87)
Unit cell parameter (Å)	a = 9.896789, b = 9.896789, c = 2.858395, Z = 16
Unit cell volume (Å^3)	279.970

Table 2
Atomic positions analyzed by Rietveld refinements for α-MnO_2.

Atoms	*x*	*y*	*z*	Occupancy
Mn1	0.34711	0.16773	0	0.46305
O1	0.16612	0.21608	0.0080	0.57308
O2	0.14609	0.50283	0.0080	0.57284

of manganese and oxygen elements is noticed without any impurities [42].

3.2. Electrochemical behavior of the as-prepared α-MnO_2 electrode

For evaluating the electrochemical behavior of α-MnO_2, and its mechanism for storing energy, the electrode was examined in a three-electrode system where the supercapacitive activities of α-MnO_2 nanorods were analyzed by cyclic voltammetry (CV) technique. The CV curves of α-MnO_2 within the sweeping rate scale of 5–100 mV/s in a potential range from 0 to 0.8 V are found in Fig. 4(a). The related non-linear and identical CV plots demonstrate the pseudocapacitive mechanism of the active α-MnO_2 electrode. Indeed, the pseudocapacitance of α-MnO_2 is considered to be representative of a fast redox process that takes place on or near the electrode surface rationalized by the intercalation of M^+, as described below [43]:

$$(MnO_2)_{Surface} + M^+ + e^- \leftrightarrow (MnOOM)_{Surface} \quad (3)$$

$$(MnO_2)_{Bulk} + M^+ + e^- \leftrightarrow (MnOOM)_{Bulk} \quad (4)$$

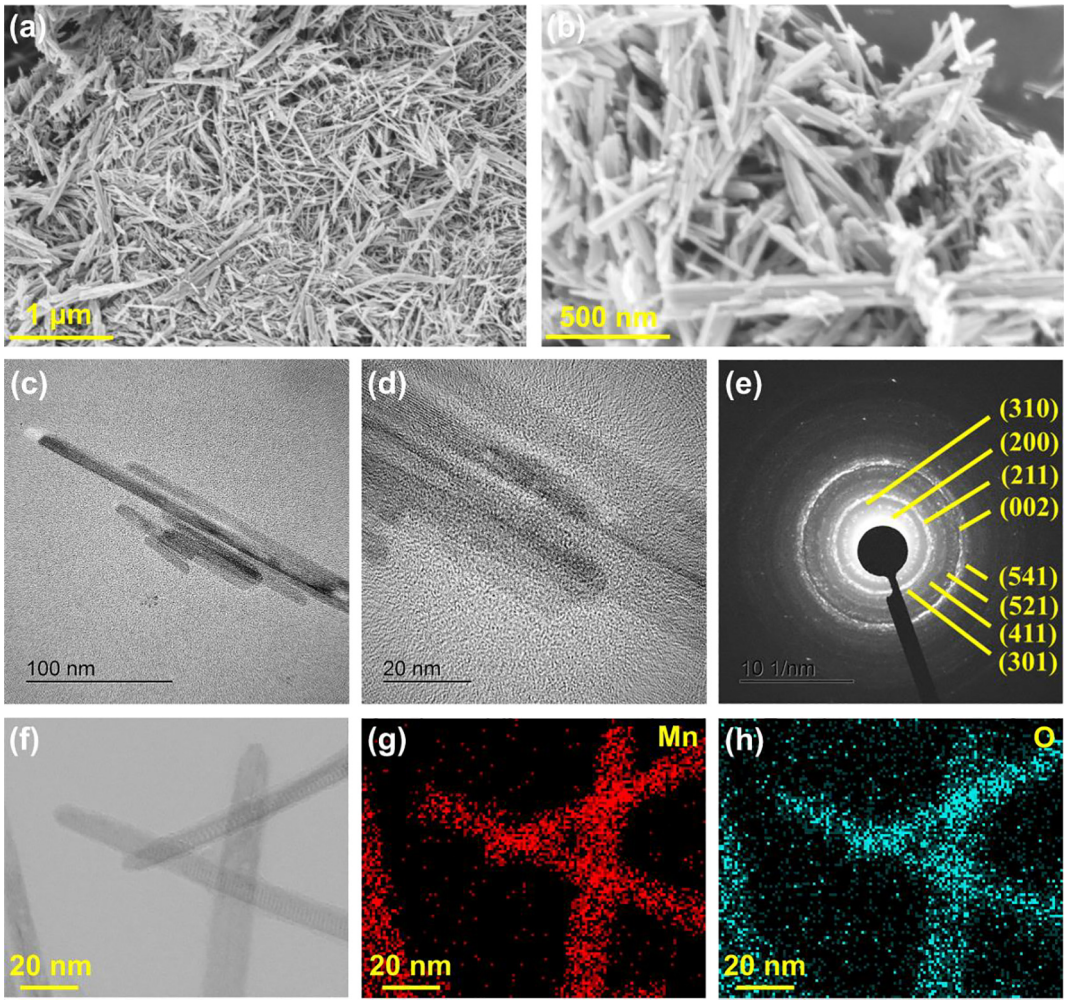

Fig. 3. (a and b) FESEM images of α-MnO_2 at 1 μm and 500 nm magnifications. (c and d) HRTEM images. (e) SAED pattern. (f–h) EDS mapping for the as-developed MONRs; the red refers to manganese (Mn), and the blue is assigned for oxygen (O).

where M^+ represents protons or alkali ions such as Na^+, Li^+, and K^+. Despite, the two above-mentioned processes describe a reversible faradic reaction by which the oxidation state of manganese ions was changed between IV and III, the first equation is assigned for the desorption/adsorption of electrolyte ions on the outer electrode surface, and the second equation is related to the insertion and extraction of these ions inside the electrode bulk. Our developed α-MnO_2 crystal lattice is formed from linking the double chains of edge-sharing MnO_6 octahedra at the corners for obtaining (2 × 2)+(1 × 1) tunnel-type structure as shown in Fig. 4(b). It is pertinent to note that sodium ions dissociated from Na_2SO_4 can act as efficient guest cations to be easily intercalated/deintercalated through the (2 × 2) tunnel structure of α-MnO_2 [44,45].

Interestingly, by utilizing the porous structure of MONRs, the as-fabricated α-MnO_2 electrode can store electrochemical energy by exhibiting capacitance of 490 F/g at the sweeping rate of 5 mV/s. While at high scan rate (200 mV/s), it still shows a well uniform reversible CV pattern, and the capacitance was detected as 267.4 F/g confirming the excellent retention rate of the electrode (Fig. 4c). The diminution in capacitance of the electrode with the rise in sweeping rate is because of the retardation of electrochemical reactions that take place when portions of the electrode surface are not accessible at higher scans. But, the capacitance gained at comparatively low scans is supposed to be due to the complete consumption of electroactive surface [46].

Importantly, the charge storage performance of the electrical charge acted by pseudocapacitive electrodes can be related to two components; the first is the diffusion component where it happens by the insertion of electrolyte ions into the material resulting in the occurrence of reversible redox reaction on theactive sites of electrode, and the second one is the capacitive behavior coming from the charge storage capacity associated with ion adsorption/desorption to the electroactive surface [47]. For better estimating the contribution of every component from the total capacitance of α-MnO_2 electrode, CV curves were utilized to obtain the functional relation among current response and scanning rate as follows:

$$i = k_1 v + k_2 v^{\frac{1}{2}} , \tag{5}$$

$$\frac{i}{v^{\frac{1}{2}}} = k_1 v^{\frac{1}{2}} + k_2 , \tag{6}$$

where k_1 and k_2 constants can be calculated from the slope and intercept of the linear plot of $i(V)/v^{1/2}$ vs. $v^{1/2}$. The associated slope and y-axis intercept are supposed to be indicative for the capacitive and diffusive currents, respectively [48]. The $i(V)/v^{1/2}$ vs. $v^{1/2}$ plot calculated for α-MnO_2 electrode has been evaluated to differentiate the redox and capacitive manners during the faradic process. After calculating, the ratios of diffusion and capacitive behaviors of MnO_2

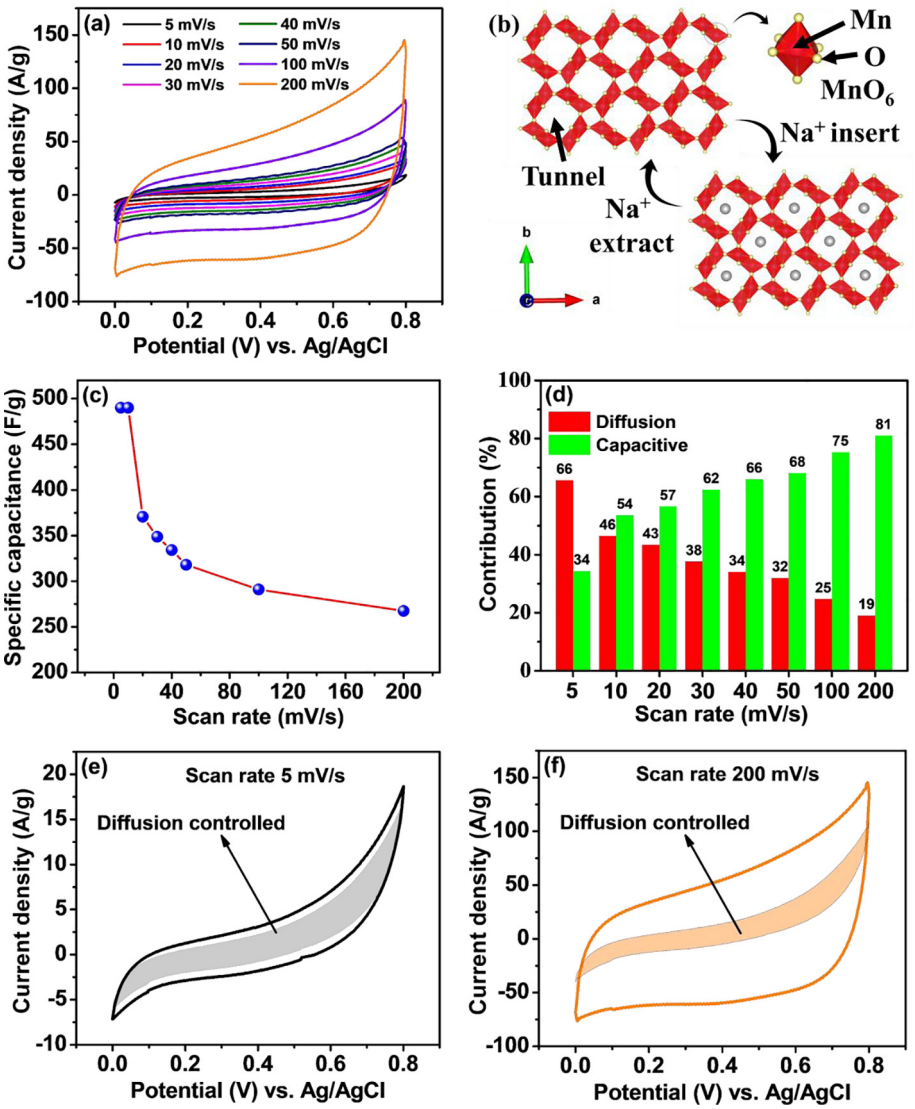

Fig. 4. Electrochemical performance of α-MnO_2 electrode. (a) CV patterns for different scan rates. (b) Charge storage mechanism related to crystal structure. (c) Specific capacitance at various scan rates. (d) Contribution ratio of diffusion/capacitive charges against various scan rates. (e and f) Separation of diffusion/capacitive contribution at scan rate of 5 and 200 mV/s.

electrode shown in Fig. 4(d–f) present the separation of capacitive (k_1v, green area) and diffusion ($k_2v^{1/2}$, red area) currents for α-MnO_2 electrode at 5 and 200 mV/s. It is perceived that the contribution of diffusion part for α-MnO_2 electrode minimizes with raising the scan rate where it was recorded as 66% at 5 mV/s and 19% at 200 mV/s because the time at the high scan rate is enough for undergoing the diffusion/intercalation of electrolyte ions inside the electrode channels [49]. Normally, researchers calculate the diffusive and capacitive contributions manually by considering very limited data points, leading to overestimation/underestimation in the measurement results. That is why we used the standard Python numerical packages in our program (script) to calculate precisely without excluding any datapoints in the current contributions. The integration of this calculation process is novel and provides a more insight approach whether calculating the dual-charge storage contributions from CV current response. CV curve deviates significantly from the orthodox rectangular shape at the lower scan rate of 5 mV/s (Fig. 4e). Moreover, the CV of the electrode shows slow current reversals at the end of potential limit as the α-MnO_2 electrode faces a high polarization resistance [50]. Additionally, the CV shapes of the pure α-MnO_2 are non-rectangular with redox activities because of the associated internal resistances and diffusion limitations of electrolyte ions of the electrode [51].

The Galvanostatic charge–discharge (GCD) curves of the α-MnO_2 with the hierarchical nanoporous structure were obtained at constant current densities from 1–10 A/g and shown in Fig. 5 (a). The non-linear charge–discharge patterns represent a rapidly reversible redox mechanism between Na^+ ions and α-MnO_2 nanorods during electrochemical reactions. Apparently, the observed non-triangular GCD curves are well-matched with the CV curves. It is observed that the change in the applied current density on the electrode causes a significant alteration in the function of iR drop where the lower values of current density have minimum iR drops. The Coulombic efficiency of the electrode attains 45% at 1 A/g, but significantly increases to 79% at 8 A/g (Table S1). The reasons behind lower Coulombic efficiencies are principally attributed to the points including the transport of soluable ions through the membrane and unfinished intercalation process to the electrode at the discharge step, resulting in less release of capacitance at the end of full discharge [52]. However, the Coulombic efficiency progressively rises with the rise in the associated current density because of the shorter time for the crossover of soluble active spe-

cies [53]. In addition, parameters such as discharge time, operating potential, associated mass loading of electrode, and applied current density are involved for obtaining the capacitance of the fabricated electrode as displayed in Fig. 5(b). The estimated capacitance of the porous α-MnO_2 electrode is 577.7 F/g at the current density of 1 A/g with a prolonged discharge time. Over and above, the electrode achieved a maximum capacitance of 213 F/g at a comparatively higher current density of 10 A/g by acquiring capacitive retention of 37%, suggesting the good rate capability of α-MnO_2 obtained from the excellent surface area and numerous active sites easily accessible to the electrolyte ions. Table 3 reveals a comparison between various electrochemical systems containing MnO_2 electrodes with our developed electrode [54–60]. It was motivating that our fabricated electrode with MONRs architecture shows a high capacitance performance compared with other previous reports.

Cycling steadiness is also a critical aspect for evaluating the supercapacitor electrode to be further applied in practical applications. The cycle life test for the α-MnO_2 electrode was analyzed at an applied current density of 10 A/g for 10,000 repetitive GCD cycles as demonstrated in Fig. 5(c). Remarkably, the electrode demonstrates much better cycling performance, thanks to hierarchical structures of α-MnO_2 nanorod morphology. It achieves capacitance retention of 98.1% after performing 10,000 cycles. Importantly, the cycling stability of the electrode suggests that conductive hierarchical porous structure helps in stabilizing the α-MnO_2 nanostructure and firmly attaching to the substrate together during the electrochemical process for lowering the degradation and film detachment from the substrate into the electrolyte clarified as common reasons for the fade of cycling life of MnO_2-based electrodes revealed in literature. The inset of Fig. 5(c) displays the GCD plots at first and last 10 cycle numbers, revealing a good symmetry and reproducibility, further confirming the superior redox reversibility.

The charge transfer mechanism of the synthesized materials was studied by executing electrochemical impedance spectroscopy (EIS) in 1 M Na_2SO_4. Fig. 5(d) depicts the Nyquist plot of α-MnO_2 electrode obtained from 100 kHz to 0.01 Hz frequency range by applying an amplitude of 0.4 V. Some parameters can be extracted from the Nyquist curve such as solution resistance (Rs) which can be expressed through the *X*-axis intercept [61] and the electrode was accurately found to have a lower Rs value (4.9 Ω), signifying

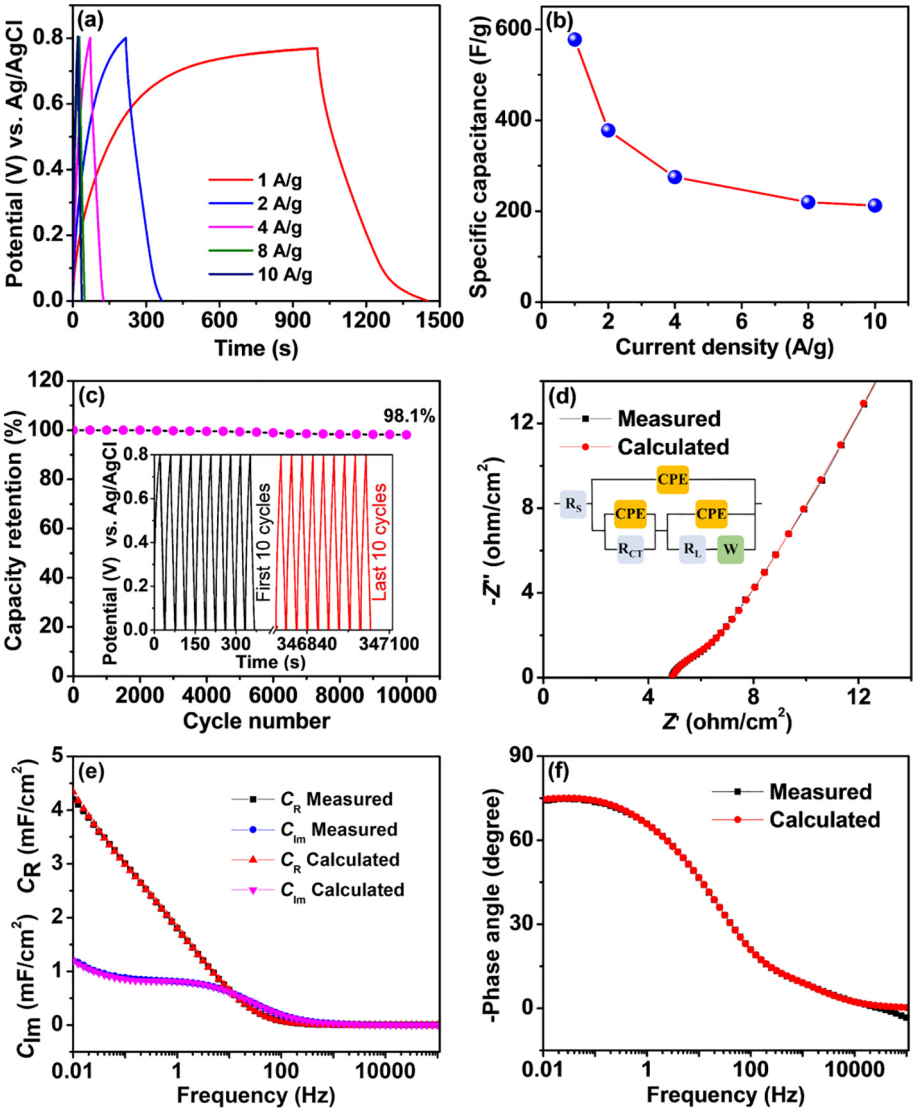

Fig. 5. (a) Galvanostatic charge–discharge curves for the as-prepared α-MnO_2 electrode. (b) Related specific capacitance at various current densities. (c) Cyclic stability for 10,000 cycles at an applied current of 10 A/g, inset displays the first and last 10 charge–discharge cycles. (d) Nyquist plot established at 0.01 Hz to 100 kHz with equivalent circuit. (e) The relationship of real and imaginary capacitance against the frequency. (f) Bode plot.

Table 3
Comparison of the electrochemical parameters of MnO_2 based systems.

Electrode materials	Electrolyte	Current density (A/g)	Specific capacitance (F/g)	Capacitance retention (%)	Ref.
MnO_2	1 M Na_2SO_4	1	262	91.3 [2000]	[54]
MnO_2 nanosheet	1 M Na_2SO_4	1.2	206.2	18.5 [4000]	[55]
BN-MC/α-MnO_2	1 M Na_2SO_4	1	338	95.6 [2000]	[56]
α-Fe_2O_3/MnO_2	1 M KOH	1	216	89.2 [1000]	[57]
MnO_2/Graphene	1 M Na_2SO_4	1	398.8	80 [5000]	[58]
MnO_2	1 M Na_2SO_4	1	297.8	95.92 [5000]	[59]
α-MnO_2 nanorods	1 M Na_2SO_4 + 0.5 M KOH	1	570	80 [10000]	[60]
α-MnO_2 nanorods	1 M Na_2SO_4	0.5	577	98.1 [10000]	Our work

the high conductivity of α-MnO_2 electrode by facilitating the access of electrolyte ions into the electroactive sites. Additionally, a clear semicircle was identified in high to mid-frequency region, giving a charge transfer resistance (R_{CT}) = 1.4 Ω, and a sloping vertical line was detected in low-frequency section, confirming the real capacitive activities of electrode [62]. Warburg impedance is an essential factor that defines the diffusion of electrolyte ions by measuring the related electrode and diffusion resistance. The data of impedance were further evaluated using the fitting method of complex nonlinear least-squares (CNLS) according to the Randles equivalent circuit (inset of Fig. 5d). From the fitting data, the constant phase element (CPE) parameter was happened because of other inseparable influences such as the variance in relaxation time, and associated diffusion disturbances because of the unfavorable inhomogeneity in the electrode porosity, at the electrode–electrolyte interface, and the electrolyte itself. As the redox behavior of α-MnO_2 is mainly caused by the ions intercalation/deintercalation, the three CPE elements noticed in the open circuit shown in Fig. 5(d) are due to semi-infinite intercalation of Na^+ ions, and electrode porosity. The leakage resistance (R_L) signifies that leakage occurring to the current flow through the double layer found at the electrode–electrolyte interface [63].

Frequency dependent real (C') and imaginary capacitive (C'') parts are graphically drawn in Fig. 5(e). Here C' refers to the accessible capacitance obtained at its corresponded frequency, meanwhile, C'' characterizes the energy dissipation because of the unfavorable irreversible process (resistive loss). The relationship of C'' against frequency reaches at the characteristic frequency (f_0) value of 6.3 Hz which is associated to analyze the relaxation time constant from $\tau_0 = 1/f_0$ = 158.7 ms; implying that the half value of cell capacitance can be obtained within a short time of 158.7 ms at low-frequency value [64].

Bode plot is a relation among the impedance phase angle and frequency as displayed in Fig. 5(f). The ideal capacitor is supposed to have a phase angle of − 90°, However, there is a resistive component in the whole electrochemical process particularly at higher frequency values (R vs. $1/j2\pi C$) that can remarkably decrease the phase angle and make the electrode to be similar in behavior to a resistor [65]. Interestingly, the plot of our electrode fabricated with MONRs surface architecture shows a phase angle value of − 74.8° that is very close to − 90°, approving impressive capacitance behavior [66]. In extension, the capacitive response frequency (f_0) for the as-fabricated α-MnO_2 electrode is obtained from the Bode plot by pointing the frequency at a phase angle of − 45° and recorded as 11.4 Hz [67]. This frequency is also used to get a response time ($\tau_0 = 1/f_0$) which is so low as 87.7 ms, further ratifying the rapid charge/discharge rates of our electrode.

3.3. Electrochemical behavior of the device

For further evaluation of the fascinating merits of as-prepared α-MnO_2, an aqueous symmetric supercapacitor device was fruitfully fabricated by assembling α-MnO_2 electrodes in a symmetrical two-electrode configuration in 1 M Na_2SO_4 electrolyte [68,69]. It was vital to select the suitable operating potential window for obtaining enhanced electrochemical features of the assembled MnO_2//MnO_2 supercapacitor device. Fig. 6(a) demonstrates the CV patterns of the fabricated SSC device operated in voltage windows of 0.8 upto 1.8 V at the sweeping rate of 50 mV/s. Decadent redox peak can be notified below 1.4 V, illustrating incomplete faradic processes that occur on the surface of the electrode. Upon reaching 1.6 V, well-defined faradic peaks are appeared, confirming the SSC cell can undergo full faradic processes with excellent reversibility. Fig. 6(b) shows CV plots of the SSC cell at different scan rates at 1.6 V. Considerably, the integral area for the cyclic voltammetry patterns is progressive with the rise in sweeping rate, clearly indicating the good capacitance behavior of the device.

GCD patterns for the as-prepared SSC device are presented in Fig. 6(c) at various current densities beginning from 0.5 to 8 A/g, exhibiting the non-triangular shapes as expected. Additionally, it can be seen that the time of charging was approximately the same as the discharge time at each specified current density describing the device with a superb Coulombic efficiency. The results (Table S1) show that Coulombic efficiency reduces with the rise in current density because of asymmetric distribution of voltage in positive and negative electrodes and associated side reactions of the fabricated device [70]. Moreover, running a device above or near to its extreme functional voltage can result in having low efficiencies because of irreversible reactions in the device as well [71].

The total specific capacitances (for the total mass of both electrodes) measured for the SSC are depicted in Fig. 6(d) in relation to the applied current density. It is motivating that the capacitance is recorded as maximum as 163.5 F/g when the current density is adjusted at 0.5 A/g and still remains 41 F/g at 8 A/g, which is superior to those similar SSC devices as reported previously (Table 4). The lower capacitance at relatively high current densities is mainly because of the major involvement of Ohmic drop and slower electrochemical kinetics. Most of the as-prepared nanostructured material cannot be efficiently participated in the electrochemical reactions by electrolyte ions at high current densities because of less association of time, resulting in low capacitance value. It can also be described in another way that the effective thickness (and morphology) of the originated electrical double-layer (EDL) affects strongly the density of adsorbed ions and the activation energy for high values of pseudocapacitance [72,73]. In other meaning, the effective thickness of the EDL, acting as a virtual membrane and separating the dissolved ions priorities, decreases along with the rise of the charging current, resulting in a reduced capacitance.

Furthermore, the MnO_2//MnO_2 aqueous symmetric cell demonstrates a maximum energy density of 58.1 Wh/kg and power density of 0.4 kW/kg at 0.5 A/g current density as specified in Ragone plot (Fig. 6e). As per the rise of current density up to 8 A/g, the energy density can still be maintained as 14.5 Wh/kg with an excellent power density of 6.4 kW/kg. The electrochemical performance of as-assembled MnO_2//MnO_2 SSC device is much higher or comparable to other previously developed aqueous symmetric

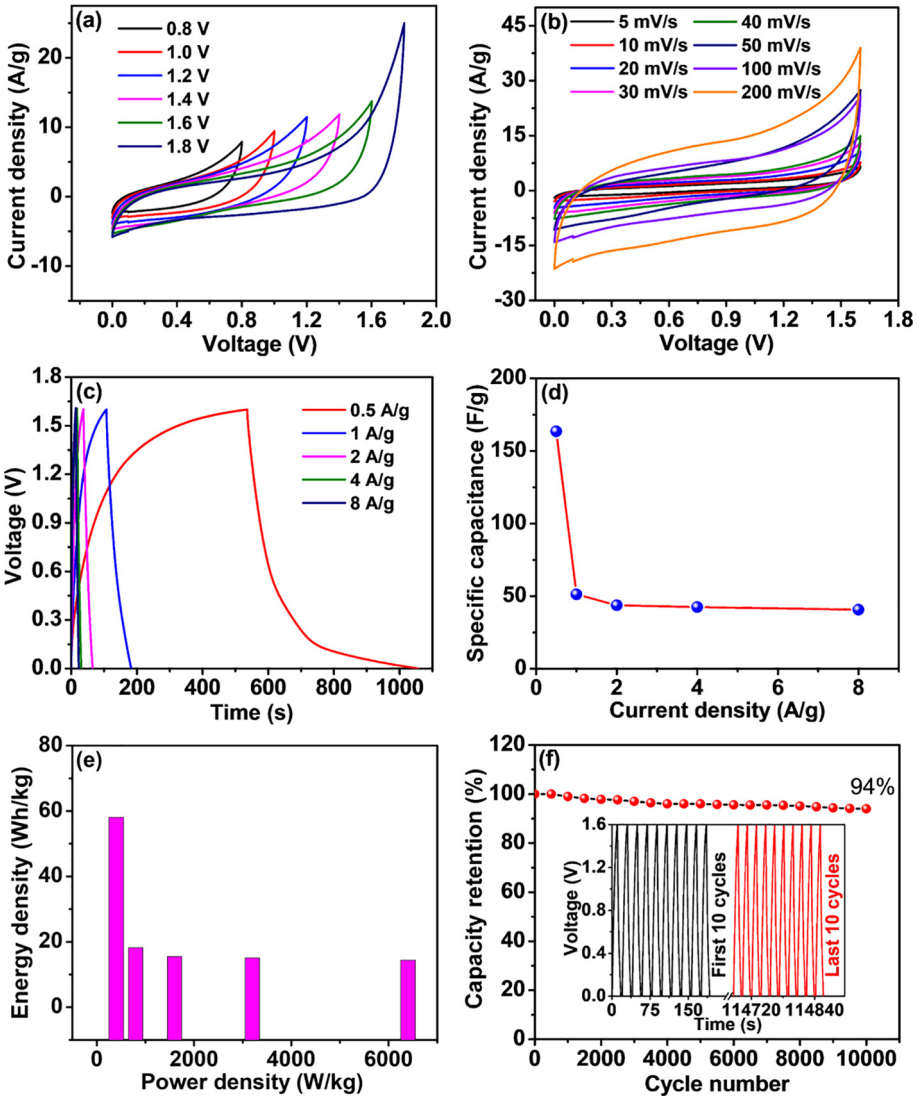

Fig. 6. Electrochemical performance of the as-assembled SSC device using α-MnO_2. (a) CV patterns performed with various voltage windows ranging at a sweeping rate of 50 mV/s. (b) CV curves at scan rates ranging from 5 to 200 mV/s with a functional window of 1.6 V. (c) GCD curves by applying constant current density ranging from 0.5 to 8 A/g. (d) Specific capacitance against various current densities. (e) Ragone plot for the as-assembled device. (f) Cycling life test performed at an applied current density of 8 A/g, inset displays the first and last 10 charge–discharge cycles.

Table 4
Summary of supercapacitor cell performance compared to other reported devices.

Electrode	Method	Cell type	Electrolyte	Specific capacitance (F/g)	Energy density (Wh/kg)	Power density (kW/kg)	Capacitance retention (%)	Refs.
MnO_2//FeOOH	Calcination	Asymmetric	1 M Li_2SO_4	51	24	0.450	85 [2000]	[74]
α-MnO_2 nanorods	DC reactive sputtering	Symmetric	1 M Na_2SO_4	194.23	4.2	0.151	89.83 [5000]	[75]
MnO_2/CNT	Annealing	Symmetric	0.1 M Na_2SO_4	44	2.9	-	100 [1000]	[76]
MnO_2	Chemical precipitation	Symmetric	2 M KNO_3	160	1.9	3.8	78 [1000]	[77]
CNT@MnO_2/CFC	Electrochemical method	Asymmetric	0.5 M Na_2SO_4	50	27.8	0.25	84 [10000]	[78]
α-MnO_2	Hydrothermal method	Symmetric	1 M Na_2SO_4	163.4	58.1	0.4	94 [10000]	Our work

supercapacitors containing manganese dioxide as described in Table 4 [74–78].

For the real-world application, the long-term stability of the symmetric cell has been investigated by performing GCD test for 10,000 cycles at constant current density of 8 A/g as shown in Fig. 6(f). The supercapacitor device delivers exceptional cyclic stability with capacitance retention of around 94.1%, confirming that the symmetric cell does not suffer any important structural

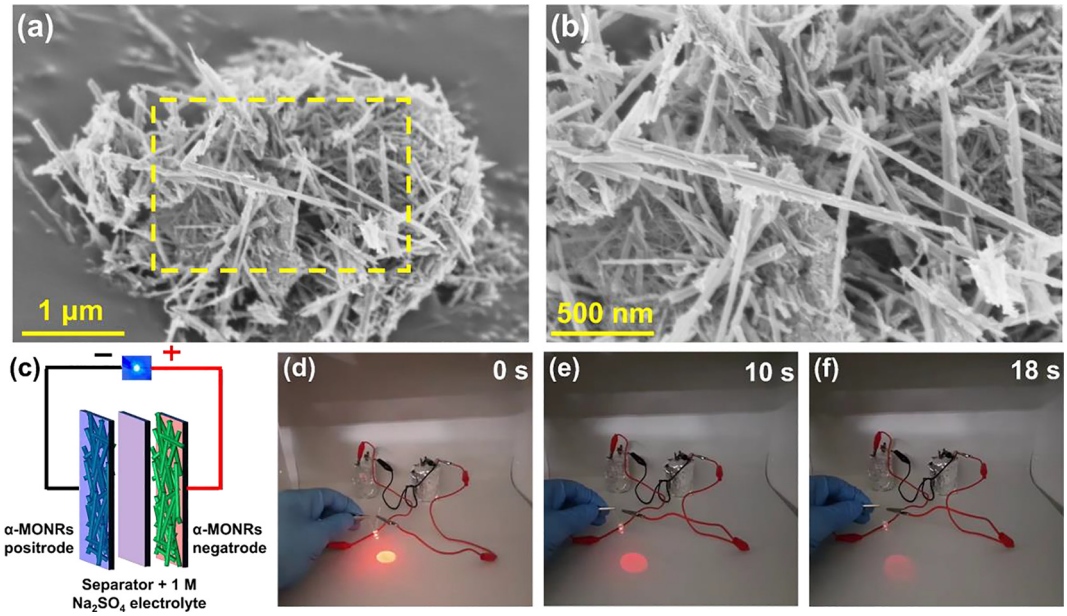

Fig. 7. (a and b) FESEM images of α-MnO_2 after cyclic stability studies. (c) Schematic representation for fabricating symmetrical α-MnO_2 device. (d–f) Photograph of symmetric supercapacitor device connected in series with red LED.

degradation throughout the continuous charge–discharge cycles. GCD plots for the last 10 cycles are similar to the first 10 cycles (inset of Fig. 6f), which verify the excellent cycling stability of the symmetric cell.

The FESEM image after 10,000 cycles is depicted in Fig. 7(a and b). Small degradation cannot be excluded as per the penetration electrolyte ions, but the initial structure remains intact which shows the strong synergistic effect [79]. Such unique nanorod structure possesses outstanding adaptability to the contraction and volume expansion in the course of cycling, altogether demonstrating in the highly stable nature of the supercapacitor [80–83]. Two electrode construction assembled by both the negative and positive electrodes has been schematically demonstrated in Fig. 7 (c). For better examining the applicability of the as-made device for real-time uses, two SSC devices containing α-MnO_2 were electrically linked in series and charged at 1 mA to glow a red light-emitting diode (LED) whose minimum working potential is 2 V as shown in Fig. 7(d–f). The LED is lightened for 18 s with a great intensity, and the intensity of its illumination decreases when the potential drops to 2 V (see Supporting video). Hence, the fabricated SSC prototype is a suitable device for real-time applications.

4. Conclusions

An eco-friendly, new, and controllable approach for the preparation of MONRs has been introduced using hydrothermal reaction for the application of supercapacitor. The developed electrode attains a maximum specific capacitance of 577.7 F/g with an excellent cycle life when it is used for 10,000 cycles because of the porous morphology of α-MnO_2 electrode that facilitates the movement of electrolyte ions into the bulk. When the aqueous symmetrical supercapacitor device is successfully assembled by utilizing the α-MnO_2, a superior capacitance of 163.5 F/g and energy density of 58.1 Wh/kg at 0.5 A/g current density are obtained with an enlarged voltage frame of 1.6 V. Moreover, the device has exceptionally withstand the cycling of 10,000 times with capacitance retention of 94.1% including the ability to light a red LED for 18 s. Such findings recommend the developed electrode material for being applied in future energy storage technologies.

Declaration of Competing Interest

The authors declare that they have no known competing financial interests or personal relationships that could have appeared to influence the work reported in this paper.

Acknowledgments

B.P. acknowledges the CONEX-Plus programme funded by Universidad Carlos III de Madrid (UC3M) and the European Commission through the Marie-Sklodowska Curie COFUND Action (Grant Agreement No 801538). The research is supported by the National Research Foundation of Korea Grant funded by the Korean Government (NRF-2019R1I1A3A0106383312). Authors gratefully acknowledges to Aliou Diatta and Abdolkhaled Mohammadi, Université de Montpellier (France) for their help in this work. The authors thank the Researchers Supporting Project (RSP-2021/55), King Saud University, Riyadh, Saudi Arabia, for financial support. The authors also appreciate financial support from Taif University Researchers Supporting Project number (TURSP-2020/135), Taif University, Taif, Saudi Arabia.

Appendix A. Supplementary data

Supplementary data to this article can be found online at https://doi.org/10.1016/j.jechem.2021.05.028.

References

[1] E.S Goda, E.S. Hong, K.R. Yoon, J. Alloys Compd. 859 (2021) 157868.
[2] H. Zhao, Q. Wu, S. Hu, H. Xu, C.N. Rasmussen, Appl. Energy 137 (2015) 545–553.
[3] C. Tang, M.-M. Titirici, Q. Zhang, J. Energy Chem. 26 (2017) 1077–1093.
[4] J. Zhou, H. Xiao, W. Weng, D. Gu, W. Xiao, J. Energy Chem. 50 (2020) 280–285.
[5] J.-X. Chen, X.-Q. Zhang, B.-Q. Li, X.-M. Wang, P. Shi, W. Zhu, A. Chen, Z. Jin, R. Xiang, J.-Q. Huang, Q. Zhang, J. Energy Chem. 47 (2020) 128–131.
[6] R. Dhilip Kumar, S. Karuppuchamy, Ceram. Int. 40 (2014) 12397–12402.
[7] S.P. Lim, N.M. Huang, H.N. Lim, Ceram. Int. 39 (2013) 6647–6655.

[8] Q.-Z. Zhang, D. Zhang, Z.-C. Miao, X.-L. Zhang, S.-L. Chou, Small 14 (2018) 1702883.
[9] M.H. Abu Elella, E.S. Goda, S.E. Hong, B. Pandit, S. Lee, H. Gamal, A. Rehman, K.R. Yoon, J. Environ. Chem. Eng. 9 (2021) 104702.
[10] J. Lee, E.S. Goda, J. Choi, J. Park, S. Lee, J. Nanopart. Res. 22 (2020) 256.
[11] E.S. Goda, K.R. Yoon, S.H. El-sayed, S.E. Hong, Thermochim. Acta 669 (2018) 173–184.
[12] E.S. Goda, M.H. Abu Elella, S.H. Hong, B. Pandit, K.R. Yoon, H. Gamal, Cellulose 28 (2021) 5087–5105.
[13] M.H. Abu Elella, E.S. Goda, H.M. Abdallah, A.E. Shalan, H. Gamal, K.R. Yoon, Int. J. Biol. Macromol. 167 (2021) 1113–1125.
[14] S. Yan, K.P. Abhilash, L. Tang, M. Yang, Y. Ma, Q. Xia, Q. Guo, H. Xia, Small 15 (2019) 1804371.
[15] K. Wang, H. Wu, Y. Meng, Z. Wei, Small 10 (2014) 14–31.
[16] B.S. Singu, E.S. Goda, K.R. Yoon, J. Ind. Eng. Chem. 97 (2021) 239–249.
[17] K. Qiu, Y. Lu, J. Cheng, H. Yan, X. Hou, D. Zhang, M. Lu, X. Liu, Y. Luo, Electrochim. Acta 157 (2015) 62–68.
[18] Q. Chen, J. Li, C. Liao, G. Hu, Y. Fu, O.K. Asare, S. Shi, Z. Liu, L. Zhou, L. Mai, J. Mater. Chem. A 6 (2018) 19488–19494.
[19] W. Wang, Y. Lu, M. Zhao, R. Luo, Y. Yang, T. Peng, H. Yan, X. Liu, Y. Luo, ACS Nano 13 (2019) 12206–12218.
[20] J. Rajeswari, P.S. Kishore, B. Viswanathan, T.K. Varadarajan, Electrochem. Commun. 11 (2009) 572–575.
[21] H. Shen, X. Kong, P. Zhang, X. Song, H. Wang, Y. Zhang, J. Alloys Compd. 853 (2021) 157357.
[22] X. Wang, X. Wang, W. Huang, P.J. Sebastian, S. Gamboa, J. Power Sources 140 (2005) 211–215.
[23] C. Yuan, B. Gao, L. Su, X. Zhang, J. Colloid Interface Sci. 322 (2008) 545–550.
[24] R.A. Davoglio, G. Cabello, J.F. Marco, S.R. Biaggio, Electrochim. Acta 261 (2018) 428–435.
[25] E.S. Goda, S. Lee, M. Sohail, K.R. Yoon, J. Energy Chem. 50 (2020) 206–229.
[26] J. Lv, X. Yang, H. Zhou, L. Kang, Z. Lei, Z.-H. Liu, Mater. Res. Bull. 73 (2016) 429–436.
[27] L. Li, Z.A. Hu, N. An, Y.Y. Yang, Z.M. Li, H.Y. Wu, J. Phys. Chem. C 118 (2014) 22865–22872.
[28] R. Jiang, T. Huang, J. Liu, J. Zhuang, A. Yu, Electrochim. Acta 54 (2009) 3047–3052.
[29] C. Xu, B. Li, H. Du, F. Kang, Y. Zeng, J. Power Sources 180 (2008) 664–670.
[30] Z. Yang, J. Chen, K. Yang, Q. Zhang, B. Zhang, J. Colloid Interface Sci. 570 (2020) 182–196.
[31] T. Gao, H. Fjellvåg, P. Norby, Anal. Chim. Acta 648 (2009) 235–239.
[32] T. Gao, M. Glerup, F. Krumeich, R. Nesper, H. Fjellvåg, P. Norby, J. Phys. Chem. C 112 (2008) 13134–13140.
[33] S. Cheng, L. Yang, D. Chen, X. Ji, Z.-J. Jiang, D. Ding, M. Liu, Nano Energy 9 (2014) 161–167.
[34] M. Du, Y. Bu, Y. Zhou, Y. Zhao, S. Wang, H. Xu, RSC Adv. 7 (2017) 12711–12718.
[35] Y. Fu, Q. Wei, G. Zhang, X. Wang, J. Zhang, Y. Hu, D. Wang, L. Zuin, T. Zhou, Y. Wu, S. Sun, Adv. Energy Mater. 8 (2018) 1801445.
[36] M. Li, W. Lei, Y. Yu, W. Yang, J. Li, D. Chen, S. Xu, M. Feng, H. Li, Nanoscale 10 (2018) 15926–15931.
[37] H. Wang, Q. Fu, C. Pan, Electrochim. Acta 312 (2019) 11–21.
[38] Z.-H. Huang, Y. Song, D.-Y. Feng, Z. Sun, X. Sun, X.-X. Liu, ACS Nano 12 (2018) 3557–3567.
[39] C. Li, Z. Yu, H. Liu, L. Kong, J. Mater. Sci. 53 (2018) 14525–14535.
[40] M. Huang, Y. Zhang, F. Li, L. Zhang, R.S. Ruoff, Z. Wen, Q. Liu, Sci. Rep. 4 (2014) 3878.
[41] Y. Ruan, J. Jiang, H. Wan, X. Ji, L. Miao, L. Peng, B. Zhang, L. Lv, J. Liu, J. Power Sources 301 (2016) 122–130.
[42] H. Sun, J. Pan, X. Yan, W. Shen, W. Zhong, X. Cheng, Ceram. Int. 45 (2019) 24802–24810.
[43] Y. Zhou, X. Cheng, F. Huang, Z. Sha, Z. Han, J. Chen, W. Yang, Y. Yu, J. Zhang, S. Peng, S. Wu, A. Rider, L. Dai, C.H. Wang, Carbon 172 (2021) 272–282.
[44] D. Su, H.-J. Ahn, G. Wang, J. Mater. Chem. A 1 (2013) 4845–4850.
[45] Z. Yang, D.C. Ford, J.S. Park, Y. Ren, S. Kim, H. Kim, T.T. Fister, M.K.Y. Chan, M.M. Thackeray, Chem. Mater. 29 (2017) 1507–1517.
[46] J. Yu, M. Wang, P. Xu, S.-H. Cho, J. Suhr, K. Gong, L. Meng, Y. Huang, J.-H. Byun, Y. Oh, Y. Yan, T.-W. Chou, Carbon 119 (2017) 332–338.
[47] M. Kazazi, M. Faryabi, J. Power Sources 449 (2020) 227510.
[48] S. Dong, L. Shen, H. Li, P. Nie, Y. Zhu, Q. Sheng, X. Zhang, J. Mater. Chem. A 3 (2015) 21277–21283.
[49] Y. Zhu, L. Peng, D. Chen, G. Yu, Nano Lett. 16 (2016) 742–747.
[50] F. Teng, S. Santhanagopalan, Y. Wang, D.D. Meng, J. Alloys Compd. 499 (2010) 259–264.
[51] Z. Li, J. Wang, X. Liu, S. Liu, J. Ou, S. Yang, J. Mater. Chem. 21 (2011) 3397–3403.
[52] L. Wei, L. Zeng, M.C. Wu, H.R. Jiang, T.S. Zhao, J. Power Sources 423 (2019) 203–210.
[53] H.R. Jiang, W. Shyy, Y.X. Ren, R.H. Zhang, T.S. Zhao, Appl. Energy 233–234 (2019) 544–553.
[54] B.S. Singu, S.E. Hong, K.R. Yoon, J. Energy Storage 25 (2019) 100851.
[55] B.S. Singu, K.R. Yoon, J. Alloys Compd. 695 (2017) 771–778.
[56] T. Liu, C. Jiang, W. You, J. Yu, J. Mater. Chem. A 5 (2017) 8635–8643.
[57] M. Racik K, A. Manikandan, M. Mahendiran, J. Madhavan, M. Victor Antony Raj, M.G. Mohamed, T. Maiyalagan, Ceram. Int. 46 (2020) 6222–6233.
[58] B.S. Singu, K.R. Yoon, J. Alloys Compd. 770 (2019) 1189–1199.
[59] Y.X. Zhang, M. Huang, F. Li, X.L. Wang, Z.Q. Wen, J. Power Sources 246 (2014) 449–456.
[60] M. Jayachandran, A. Rose, T. Maiyalagan, N. Poongodi, T. Vijayakumar, Electrochim. Acta 366 (2021) 137412.
[61] S. Sagadevan, A.R. Marlinda, M.R. Johan, A. Umar, H. Fouad, O.Y. Alothman, U. Khaled, M.S. Akhtar, M.M. Shahid, J. Colloid Interface Sci. 558 (2020) 68–77.
[62] S.A. Pande, B. Pandit, B.R. Sankapal, Mater. Des. 182 (2019) 107972.
[63] Z. Zeng, Y. Liu, W. Zhang, H. Chevva, J. Wei, J. Power Sources 358 (2017) 22–28.
[64] B. Pandit, S.A. Pande, B.R. Sankapal, Chin. J. Chem. 37 (2019) 1279–1286.
[65] G. Ren, X. Pan, S. Bayne, Z. Fan, Carbon 71 (2014) 94–101.
[66] S.A. Pande, B. Pandit, B.R. Sankapal, Mater. Lett. 209 (2017) 97–101.
[67] B. Pandit, A. Agarwal, P. Patel, B.R. Sankapal, Nanoscale Adv. 3 (2021) 1057–1066.
[68] S.A. Pande, B. Pandit, B.R. Sankapal, J. Colloid Interface Sci. 514 (2018) 740–749.
[69] B. Pandit, S.R. Dhakate, B.P. Singh, B.R. Sankapal, Electrochim. Acta 249 (2017) 395–403.
[70] Y. Cheng, X. Xi, D. Li, X. Li, Q. Lai, H. Zhang, RSC Adv. 5 (2015) 1772–1776.
[71] M.D. Stoller, R.S. Ruoff, Energy Environ. Sci. 3 (2010) 1294–1301.
[72] K. Bohinc, V. Kralj-Iglič, A. Iglič, Electrochim. Acta 46 (2001) 3033–3040.
[73] P. Ratajczak, M.E. Suss, F. Kaasik, F. Béguin, Energy Storage Mater. 16 (2019) 126–145.
[74] W.-H. Jin, G.-T. Cao, J.-Y. Sun, J. Power Sources 175 (2008) 686–691.
[75] A. Kumar, A. Sanger, A. Kumar, Y. Kumar, R. Chandra, Electrochim. Acta 222 (2016) 1761–1769.
[76] A.L.M. Reddy, M.M. Shaijumon, S.R. Gowda, P.M. Ajayan, J. Phys. Chem. C 114 (2010) 658–663.
[77] V. Khomenko, E. Raymundo-Piñero, F. Béguin, J. Power Sources 153 (2006) 183–190.
[78] K. Wu, Z. Ye, Y. Ding, Z. Zhu, X. Peng, D. Li, G. Ma, J. Power Sources 477 (2020) 229031.
[79] M.F. Mousavi, M. Hashemi, M.S. Rahmanifar, A. Noori, Electrochim. Acta 228 (2017) 290–298.
[80] C. Wu, Y. Zhu, M. Ding, C. Jia, K. Zhang, Electrochim. Acta 291 (2018) 249–255.
[81] M.H. Abu Elella, E.S. Goda, K.R. Yoon, S.E. Hong, M. Morsy, R. Sadak, H. Gamal, Compos. Commun. 24 (100614) (2021).
[82] B. Pandit, S.R. Rondiya, N.Y. Dzade, S.F. Shaikh, N. Kumar, E.S. Goda, A.A. Al-kahtani, R.S. Mane, S. Mathur, R.R. Salunkhe, ACS Appl. Mater. Interfaces 13 (2021) 11433–11441.
[83] E.S. Goda, M.H. Abu Elella, M. Sohail, B.S. Singu, B. Pandit, A.M. El Shafey, A.M. Aboraia, H. Gamal, S.H. Hong, K.R. Yoon, Int. J. Biol. Macromol. 182 (2021) 680–688.